

Supplementary information

High-Conversion-Efficiency and Stable Six-Electron Zn-I₂ Batteries Enabled by Organic Iodide/Thiazole-Linked Covalent Organic Frameworks

Wenyan Du,^a Qi Huang,^b Xunwen Zheng,^a Yaokang Lv,^d Ling Miao,^a Ziyang Song,^a Lihua Gan,^{a,c} Mingxian Liu^{a, c*}

^a Shanghai Key Lab of Chemical Assessment and Sustainability, School of Chemical Science and Engineering, Tongji University, 1239 Siping Rd., Shanghai, 200092, P. R. China. E-mail: liumx@tongji.edu.cn

^b Institute for Electric Light Sources, School of Information Science and Technology, Fudan University, 220 Handan Rd., P. R. China.

^c State Key Laboratory of Cardiovascular Diseases and Medical Innovation Center, Shanghai East Hospital, School of Medicine, Tongji University, 150 Jimo Rd., Shanghai 200120, P. R. China

^d College of Chemical Engineering, Zhejiang University of Technology, 18 Chaowang Rd., Hangzhou 310014, P. R. China.

Table of Contents

Section S1. Experimental Procedures.....S4

1.1 Material Synthesis.

1.2 Characterizations.

1.3 Electrochemical Measurements.

Section S2. Calculation Methods.....S7

2.1 Density Functional Theory Calculation.

2.2 Optical Energy Gap.

2.3 Activation Energy.

2.4 Proton Capacity Contribution.

2.5 Redox Electron Transfer Number.

2.6 Capacitive Contribution.

Section S3. Supplementary Characterizations.....S9

Figure S1. Thermogravimetric analysis of TZ-COFs.

Figure S2. Optimized molecular structures and ESP simulations for (a) TA, (b) ND and (c) TZ-COFs.

Figure S3. Molecular configuration of C₃H₉IS.

Figure S4. (a) Nitrogen adsorption/desorption isotherms and (b) pore size distributions of TZ-COFs and C₃H₉IS/TZ-COFs.

Figure S5. A three-electrode Swagelok cell with a Hg/HgCl₂ reference electrode.

Figure S6. (a, b) CV curve and (c, d) cycling performances of C₃H₉SBF₄ and TZ-COFs electrodes.

Figure S7. GCD curve of the active carbon additive at 1 A g⁻¹.

Figure S8. (a) EIS profiles of C₃H₉IS/TZ-COFs, C₃H₉IS/COFs and C₃H₉IS/AC electrodes.

Figure S9. (a) Cycling capacities and (b) conversion efficiency of C₃H₉IS/TZ-COFs electrode with various mass loadings.

Figure S10. Fitted b values for redox peaks of C₃H₉IS/TZ-COFs electrode

Figure S11. Capacitive contribution of C₃H₉IS/TZ-COFs electrode.

Figure S12. SEM images of C₃H₉IS/TZ-COFs electrode at different (dis)charge stages.

Figure S13. CV curves of C₃H₉IS/TZ-COFs and C₃H₉IS/COFs electrodes.

Figure S14. Self-discharge behavior of C₃H₉IS/TZ-COFs electrode at 1 A g⁻¹.

Figure S15. CV curves of C₃H₉IS/TZ-COFs electrode in Zn(OTF)₂ electrolyte.

Figure S16. CV curves of C₃H₉IS/TZ-COFs electrode in MPIBr electrolyte.

Figure S17. CV curves of C₃H₉IS/AC electrode.

Figure S18. CV and GCD curve of I₂/TZ-COFs electrode in aqueous Zn(OTF)₂ electrolyte.

Figure S19. (a) Rate capacities and (b) cycling stability of I₂/AC and I₂/TZ-COFs electrodes in Zn(OTF)₂-MPIBr electrolyte.

Figure S20. Electrochemical properties of C₃H₉IS/TZ-COFs electrode in aqueous 3 M ZnSO₄-MPIBr electrolyte. (a) CV curve, (b) rate capacities, (c) cycling stability and (d) self-discharge behavior.

Figure S21. The capacity, Coulombic efficiency and cycling stability of Zn||C₃H₉IS/TZ-COFs battery.

Figure S22. The binding energies of I₂ and C₃H₉IS with H₂O without (a, b) and with (c, d) TZ-COFs.

Figure S23. (a, b) SEM images, (c) FI-IR spectra and (d) XRD patterns of C₃H₉IS/TZ-COFs electrode before and after cycling.

Figure S24. XPS spectra of (a) N 1s and (b) S 2p, (c) *ex-situ* FT-IR spectra of C₃H₉IS/TZ-COFs electrode at different (dis)charging states, (d) Absorption/desorption mechanism of different iodine species at C=N/C-S sites.

Figure S25. S 2p XPS spectra of C₃H₉IS and TZ-COFs.

Figure S26. UV-vis absorbance spectra of TZ-COFs, COFs and AC to IO₃⁻.

Figure S27. EIS spectra of (a) C₃H₉IS/TZ-COFs and (b) C₃H₉IS/AC batteries electrode.

Table S1. Performance comparison of Zn-I₂ batteries.

Section S4. References.....S23

Section S1. Experimental Procedures

1.1 Material Synthesis.

Synthesis of thiazole-linked covalent organic frameworks (TZ-COFs):^[S1] Benzene-1,3,5-tricarbaldehyde (8.11 mg), naphthalene-2,6-diamine (11.87 mg) and sulfur (14.4 mg) were weighed into a 10 mL glass tube. Acetic acid (AcOH, 6 M, 0.10 mL), dimethyl sulfoxide (DMSO 0.05 mL), *N,N*-dimethylacetamide (0.45 mL) and mesitylene (0.50 mL) were then added into the mixture. The tube was flash frozen in a liquid nitrogen bath, evacuated to an internal pressure of 0.5 mbar and flame sealed, reducing the total length by ca. 10 cm. Upon warming to room temperature, the sealed tube was placed in an oven at 120 °C for 72 h, yielding a brown solid. The powder was collected and dried at 60 °C for 12 h to yield TZ-COFs as a brown powder (19.43 mg, 88% yield). TZ-COFs (~10 mg) was suspended in 8 mL either water, HCl (12.5 M), KOH (12 M) to test its stability. The samples were then analysed for FT-IR and XRD analysis. The comparison sample N-COFs was a sulfur-free sample, and the other synthesis steps were the same as TZ-COFs.

For C₃H₉IS/TZ-COFs preparation, the commercial organic trimethylsulfonium iodide (C₃H₉IS) was mixed with TZ-COFs with a weight ratio of 3:1 by milling. Then the mixture was sealed into the quartz tube under vacuum following with thermal treatment at 160 °C for 4 h to obtain C₃H₉IS/TZ-COFs. The comparison sample C₃H₉IS/N-COFs and C₃H₉IS/AC were prepared by using COFs and activity carbon (AC) as host, and the other synthesis steps were the same as C₃H₉IS/TZ-COFs.

1.2 Characterizations.

The sample microstructures were observed using scanning electron microscopy (SEM, Hitachi S-4800) and transmission electron microscopy (TEM, JEM-2100). Fourier-transformed infrared spectrum (FT-IR) was collected on a Thermo Nicolet NEXUS spectrometer. The material structure was characterized by X-ray diffraction (XRD, Bruker D8 advance powder diffractometer with a Cu K α radiation source). The surface chemistry was studied by an X-ray photoelectron spectrometer (XPS, AXIS Ultra DLD). Thermogravimetric (TG) analysis was performed with a STA409 PC thermogravimetric analyzer at a heating speed of 10 °C min⁻¹. The structural information was investigated by Raman spectrum (Renishaw Invia) using 514 nm laser excitation under ambient conditions. Nitrogen sorption tests were carried out using a Micromeritics

ASAP2020 physisorption analyzer at $-196\text{ }^{\circ}\text{C}$ to determine the Brunauer–Emmert–Teller (BET) specific surface area, pore volume, and pore size distribution. The surface area and pore size distribution were calculated by using the Brunauer–Emmett–Teller (BET) equation and the nonlocal density functional theory model. The ultraviolet visible (UV-Vis) spectra were collected on a JASCO V-750 UV-Vis spectrometer.

1.3 Electrochemical Measurements.

The electrode was prepared by pressing a slurry mixture containing $\text{C}_3\text{H}_9\text{IS}/\text{TZ-COFs}$ materials (70 wt%), activity carbon (AC, 20 wt%), and polytetrafluoroethylene (PTFE, 10 wt%) onto the titanium foil, and then dried at $30\text{ }^{\circ}\text{C}$. All electrochemical performance were conducted in three-electrode Swagelok cells with Hg/HgCl_2 reference electrode and Ti mesh counter electrode. All electrochemical performances were estimated when considering the mass loading of active $\text{C}_3\text{H}_9\text{IS}$ molecule (61.2 wt%) in $\text{C}_3\text{H}_9\text{IS}/\text{TZ-COFs}$ electrode ($\sim 2.5\text{ mg cm}^{-2}$). A three-electrode cell configuration (Figure S5) was employed using 2 mL $\text{Zn}(\text{OTF})_2\text{-MPIBr}$ electrolyte with an iodine-to-electrolyte ratio of 1.25 mg L^{-1} . The 3 M $\text{Zn}(\text{CF}_3\text{SO}_3)_2$ aqueous electrolyte containing 0.1 M 1-methyl-3-propylimidazolium bromide (MPIBr, 99%; Meryer) as electrolyte. The full battery was assembled using 2032 coin-type cell with Zn anode (20 mg), $\text{C}_3\text{H}_9\text{IS}/\text{TZ-COFs}$ cathode (2.5 mg) and aqueous $\text{Zn}(\text{OTF})_2\text{-MPIBr}$ electrolyte (120 μL). The N/P ratio was calculated as follows:

$$\text{N/P} = \frac{\text{Zn anode capacity}}{\text{Cathode capacity}} = \frac{20\text{ mg} \times 820\text{ mAh g}^{-1}}{2.5\text{ mg} \times 1296\text{ mAh g}^{-1}} = 5.06$$

The galvanostatic charge/discharge (GCD), rate performance and cycle stability were estimated on a LAND-CT3001A battery test system with a voltage range of 0.1–1.3 V. Cyclic voltammetry (CV) and electrochemical impedance spectroscopy (EIS) tests were performed on an electrochemical workstation (CHI660E). The specific capacity (C_m , mAh g^{-1}) was calculated from GCD curves using the following equation:

$$C_m = \frac{I \times \Delta t}{m} \quad (\text{Eq. S1})$$

where I is the current density (A g^{-1}), t is the discharging time (s), and m (g) is the mass loading of active materials ($\text{C}_3\text{H}_9\text{IS}/\text{TZ-COFs}$ composite) on the electrode. Of note, the electrochemical capacity was calculated based on the mass loading of $\text{C}_3\text{H}_9\text{IS}$ in the electrode, *i.e.* 2.5 mg cm^{-2} .

The electron transfer number (n) during the redox reaction process was calculated based on the following equation:

$$n = \frac{3.6 \times C_m \times M}{F} \quad (\text{Eq. S2})$$

where M is the molar mass of organic molecules (g mol^{-1}), F is a constant (96485 C mol^{-1}).

The gravimetric energy density (E , Wh kg^{-1}) and power density (P , W kg^{-1}) of the Zn-I₂ batteries were calculated according to the following equations:

$$E = C_m \times \Delta V \quad (\text{Eq. S3})$$

$$P = \frac{E}{1000 \times \Delta t} \quad (\text{Eq. S4})$$

where ΔV is the voltage window. It is worth noting that the electrochemical capacities and energy/power densities of the Zn-I₂ batteries were calculated based on the total mass of the C₃H₉IS/TZ-COFs composite as the active material on the electrodes.

The mass loading of C₃H₉IS in the electrode (ω) is 61.2 wt%, which is calculated by the following equation:

$$\omega = m(\text{C}_3\text{H}_9\text{IS}) / [m(\text{C}_3\text{H}_9\text{IS}) + m(\text{TZ-COFs})] \quad (\text{Eq. S5})$$

where $m(\text{C}_3\text{H}_9\text{IS})$ and $m(\text{TZ-COFs})$ represent the mass of C₃H₉IS and TZ-COFs, respectively.

Section S2. Calculation Methods

2.1 Density Functional Theory (DFT) Calculation.

Supramolecular Property Simulation. The theoretical calculations were executed via the Gaussian 16 suite of programs.^[S2] The structures of TZ-COFs and its dimer were optimized at the B3LYP-D3/ def2-SVP level of theory. The negative electrostatic potential (ESP, blue color) suggests electrophilic properties, while the positive ESP (red color) denotes nucleophilic ones. The molecular orbital levels, including the highest occupied molecular orbital (HOMO) and the lowest unoccupied molecular orbital (LUMO), and the charge population sum of TZ-COFs were studied at the B3LYP-D3/TZVP level of theory.^[S3] The solvent (H₂O) effect was included in the calculations using the solvation model based on the density (SMD) model.^[S4] The iso-chemical shielding surface (ICSS) and reduce density gradient (RDG) simulations was carried out by using Multiwfn program,^[S5] where RDG value provides interaction strength while $\text{sign}(\lambda_2)\rho$ value shows interaction types. Large and negative values of $\text{sign}(\lambda_2)\rho$ are suggestive of H-bond interactions, values near zero unravel the π - π stacking interactions. The colored gradient isosurface map intuitively exhibit the interaction area and corresponding strength. The VMD software^[S6] was employed to plot the color-filled isosurface graphs of molecular orbitals, and ICSS_{ZZ}, as well as the noncovalent interaction (NCI) maps.

Geometry optimization and Charge Density Difference: All the DFT calculations are performed by the Vienna Ab initio Simulation Package (VASP) with the projector augmented wave (PAW) method. The exchange-functional is treated using the generalized gradient approximation (GGA) with Perdew-Burke-Emzerhof (PBE) functional. The energy cutoff for the plane wave basis expansion was set to be 400 eV. Partial occupancies of the Kohn-Sham orbitals were allowed using the Gaussian smearing method and a width of 0.2 eV. The Brillouin zone was sampled with Monkhorst mesh of $1 \times 1 \times 1$ for the optimization for all the structures. The self-consistent calculations apply a convergence energy threshold of 10^{-4} eV, and the force convergency was set to be $0.05 \text{ eV } \text{\AA}^{-1}$. The charge density differences were analyzed through VASPKIT code.^[S3]

2.2 Optical Energy Gap.

The optical energy gaps (E_g , eV) of TZ-COFs, ND and TA were calculated by UV-Vis spectroscopy using the following forms:^[S7]

$$\alpha \propto \frac{(h\nu - E_g)^{1/2}}{h\nu} \quad (\text{Eq. S6})$$

$$h\nu = 1280/\lambda \quad (\text{Eq. S7})$$

where α is the optical absorption coefficient, $h\nu$ denotes the photon energy, λ is the wavelength.

2.3 Capacitive Contribution.

The ion transport kinetics of C₃H₉IS/TZ-COFs electrodes were investigated based on the relationship:^[S8]

$$i = k\nu^b \quad (\text{Eq. S8})$$

where k and b are constants, i is current density, and ν refers to scan rate. When the power exponent b value is close to 0.5, it indicates a diffusion-controlled process, while a b -value of 1.0 identifies a surface-controlled reaction.

The Dunn's method was applied to analyze the capacitance contribution from the capacitive process (rapid surface redox reactions) and the diffusion-controlled process.

Quantitative analysis for capacitive contribution can be through the following equation:

$$i = k_1\nu + k_2\nu^{1/2} \quad (\text{Eq. S9})$$

where k_1 and k_2 are constants, $k_1\nu$ and $k_2\nu^{1/2}$ represent the current density contributed from fast-capacitive process and diffusion-controlled process, respectively. Dividing $\nu^{1/2}$ on both sides of the above equation yields:

$$i/\nu^{1/2} = k_1\nu^{1/2} + k_2 \quad (\text{Eq. S10})$$

Therefore, $i/\nu^{1/2}$ and $\nu^{1/2}$ are expected to give a linear relationship, two capacity contributions can be distinguished by linear fitting. The slope corresponds to k_1 and the y-intercept equals k_2 . By repeating the above steps for other potentials and scan rates, the respective capacity contribution from the surface-dominated process and a diffusion-limited process can be quantitatively calculated.

Section S3. Supplementary Characterizations

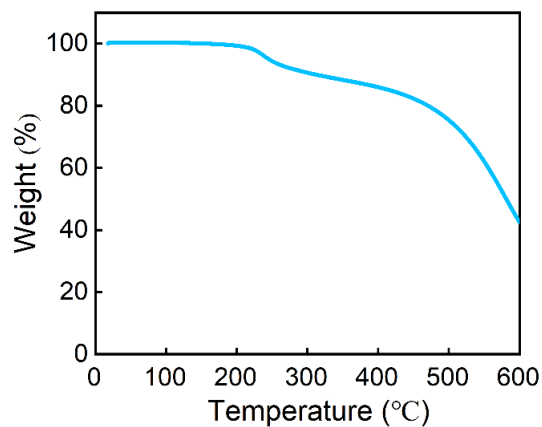


Figure S1. Thermogravimetric analysis of TZ-COFs.

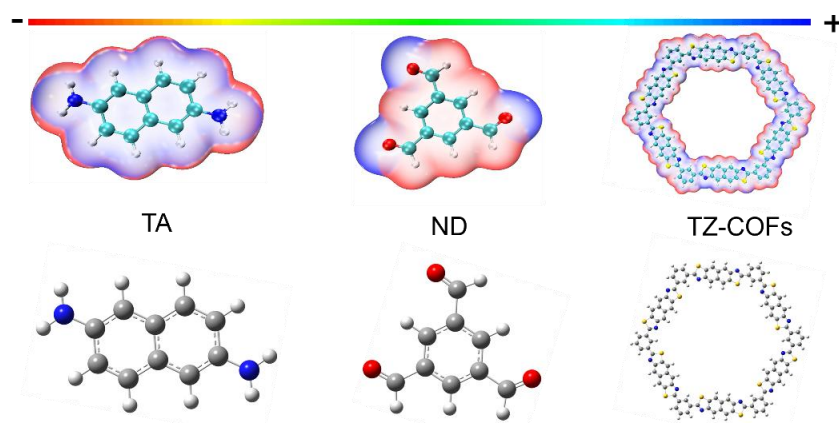


Figure S2. Optimized molecular structures and ESP simulations for (a) TA, (b) ND and (c) TZ-COFs.

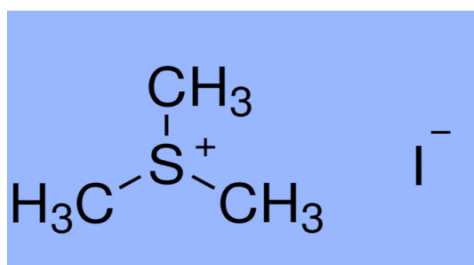


Figure S3. Molecular configuration of C₃H₉IS.

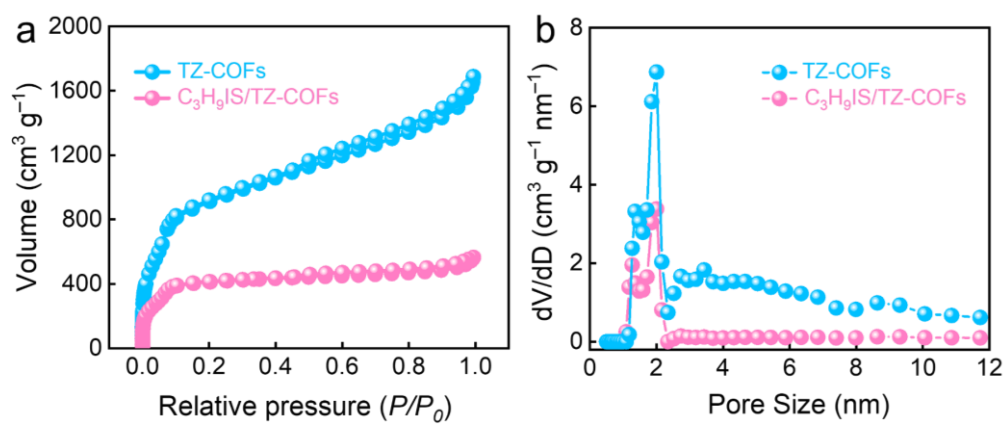


Figure S4. (a) Nitrogen adsorption/desorption isotherms and (b) pore size distributions of TZ-COFs and C₃H₉IS/TZ-COFs.



Figure S5. A three-electrode Swagelok cell with a Hg/HgCl₂ reference electrode.

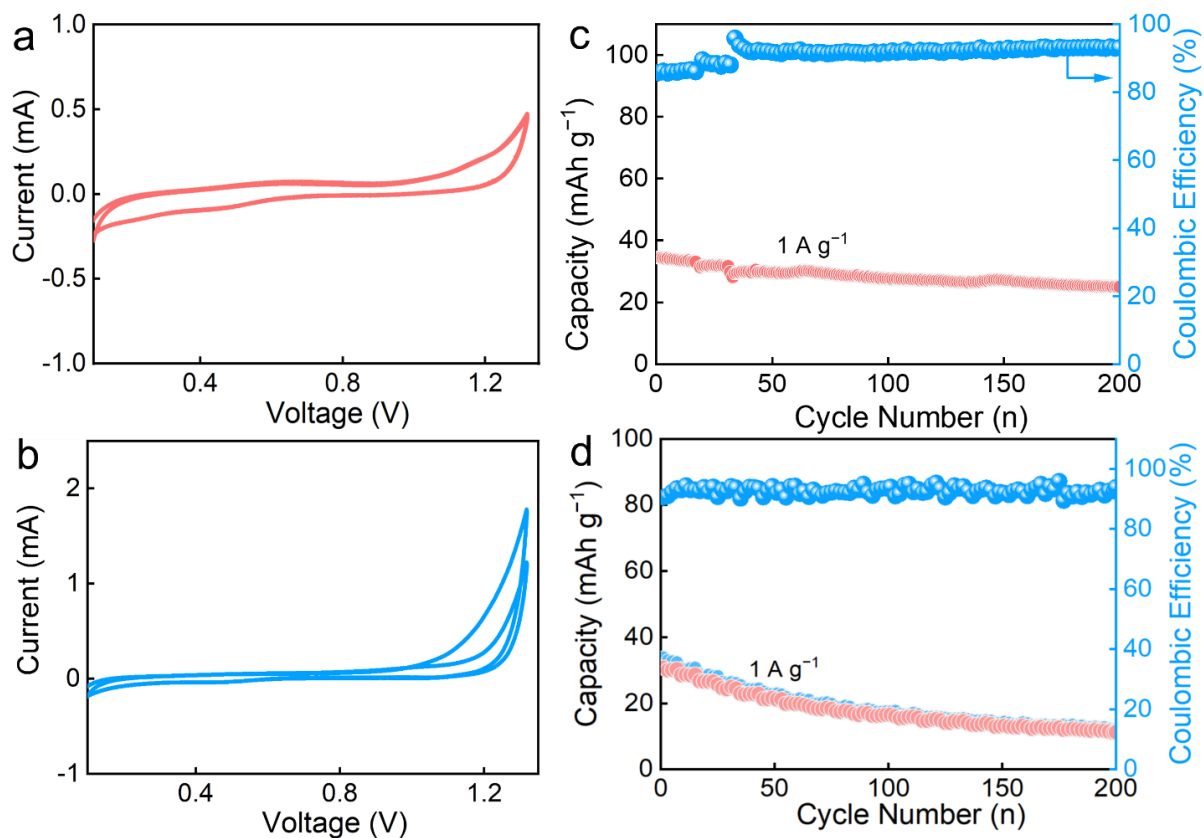


Figure S6 (a, b) CV curve and (c, d) cycling performances of C₃H₉SBF₄ and TZ-COFs electrodes.

Notes to Figure S6: Both C₃H₉SBF₄ and TZ-COFs electrodes show inferior redox behaviors in CV profiles and contribute the capacities of 38 and 34 mAh g⁻¹.

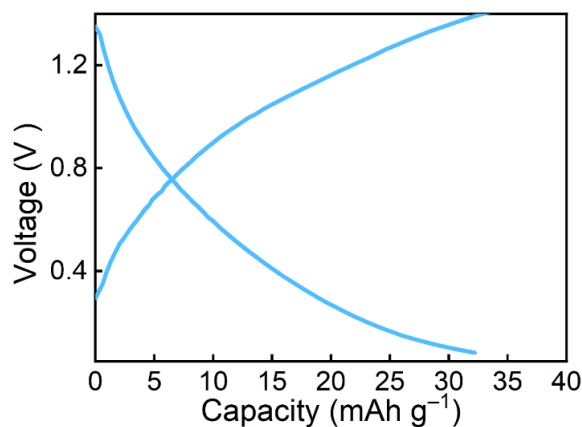


Figure S7 GCD curve of the active carbon additive at 1 A g⁻¹.

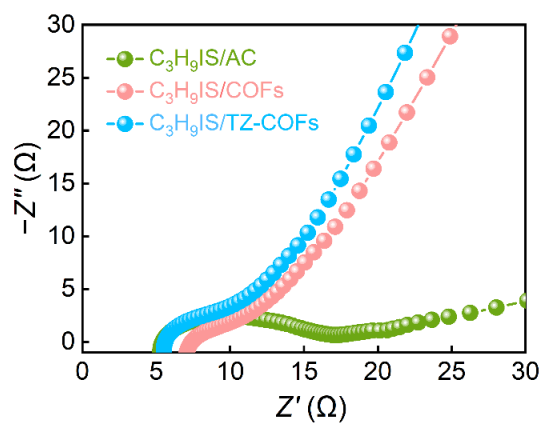


Figure S8. EIS profiles of $C_3H_9IS/TZ-COFs$, $C_3H_9IS/COFs$ and C_3H_9IS/AC electrodes.

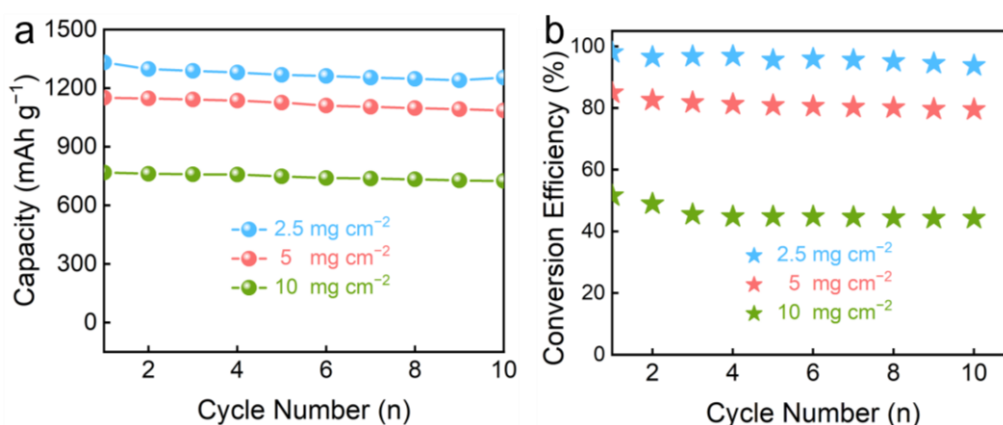


Figure S9. (a) Cycling capacities and (b) conversion efficiency of $C_3H_9IS/TZ-COFs$ electrode with various mass loadings.

Notes to Figure S9: As the mass loading of C_3H_9IS in $C_3H_9IS/TZ-COFs$ electrode increase from 2.5 to 10 $mg\ cm^{-2}$, the capacity of $C_3H_9IS/TZ-COFs$ electrode decrease from 1296 to 767 $mAh\ g^{-1}$ (Figure S9a) . This reduction corresponds to a decline in iodine conversion efficiency from 97 to 58% (Figure S9b), primarily attributed to enhanced ion diffusion resistance in thicker electrodes.

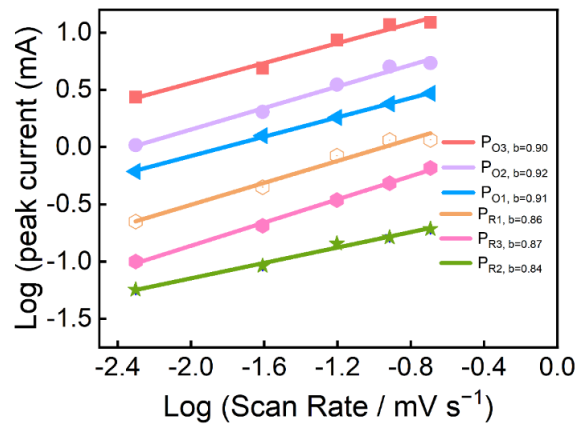


Figure S10. Fitted b values for redox peaks of $C_3H_9IS/TZ-COFs$ electrode.

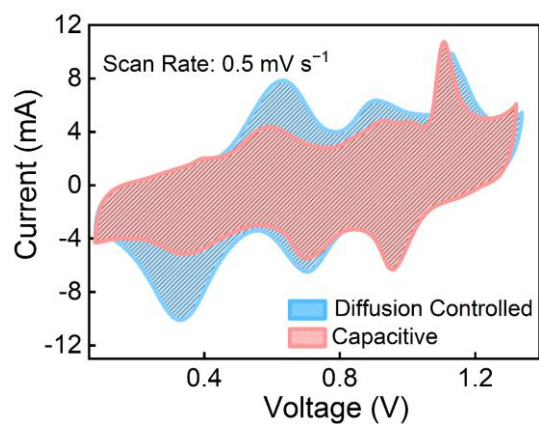


Figure S11. Capacitive contribution of $C_3H_9IS/TZ-COFs$ electrode.

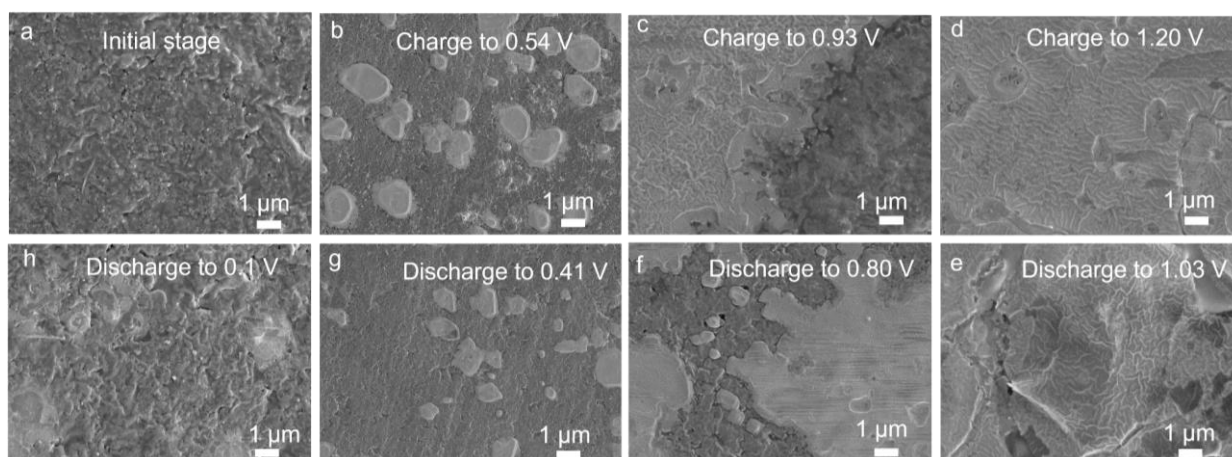


Figure S12. SEM images of $C_3H_9IS/TZ-COFs$ electrode at different (dis)charge stages.

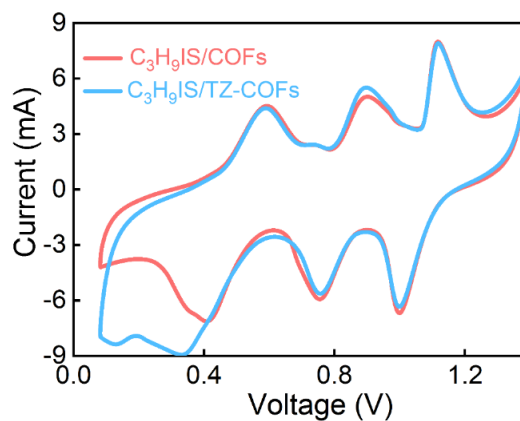


Figure S13. CV curves of $C_3H_9IS/TZ-COFs$ and $C_3H_9IS/COFs$ electrode.

Notes to Figure S13: The average discharge voltage (1.13 V) is obtained by dividing the energy density (1464 Wh kg^{-1}) by the corresponding discharge capacity (1296 mAh g^{-1}).

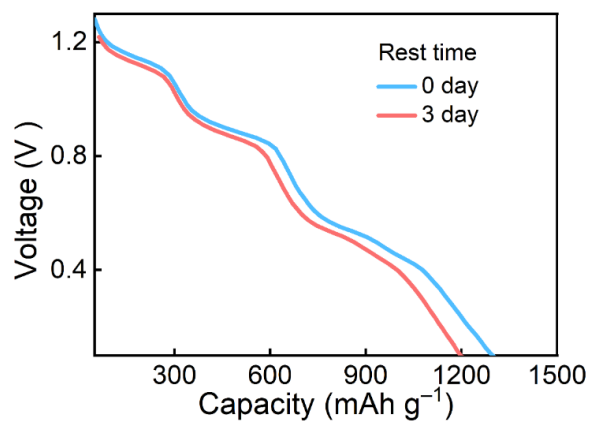


Figure S14. Self-discharge behavior of $C_3H_9IS/TZ-COFs$ electrode at 1 A g^{-1} .

Notes to Figure S14: The self-discharge behavior of Zn- I_2 battery is studied at the fully charged condition of 1.3 V, which shows a high-capacity retention of 93% after a rest step of 3 days.

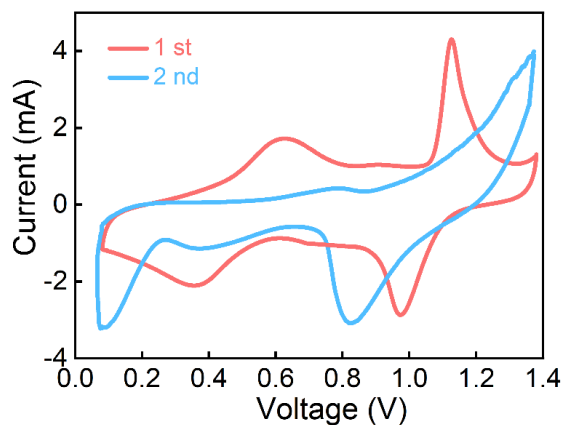


Figure S15. CV curves of $C_3H_9IS/TZ-COFs$ electrode in $Zn(OTF)_2$ electrolyte.

Notes to Figure S15: CV curve of $C_3H_9IS/TZ-COFs$ electrode in $Zn(OTF)_2$ electrolyte only display two pair of redox peaks at 0.54/0.41 V (I^-/I^0) and 1.20/1.03 V (I^0/I^{5+}) in the first cycle (Figure S15) corresponding to $I^-/I^0/I^{5+}$ conversion, together with irreversible iodine conversion process and inferior charge storage behavior in the second cycle. Such a result highlight the crucial role of MPIBr in activating I^+ to stimulate high-conversion-efficiency and stable $I^-/I^0/I^+/I^{5+}$ iodine conversion for better Zn- I_2 batteries. Thus, it is difficult to achieve $6 e^- I^-/IO_3^-$ redox process in $Zn(OTF)_2$ electrolyte without MPIBr.

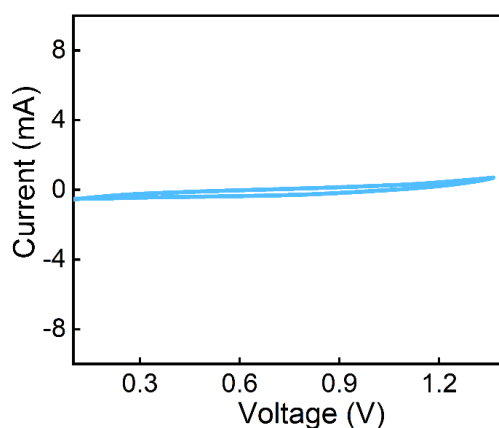


Figure S16. CV curves of $C_3H_9IS/TZ-COFs$ electrode in MPIBr electrolyte.

Notes to Figure S16: CV profile of $C_3H_9IS/TZ-COFs$ electrode in MPIBr electrolyte within the voltage range of 0.1–1.3 V shows inferior electrochemical energy storage behavior without redox signals (Figure S16). This result indicates that MPIBr does not undergo decomposition or conversion processes, showing a negligible contribution to the overall capacity.

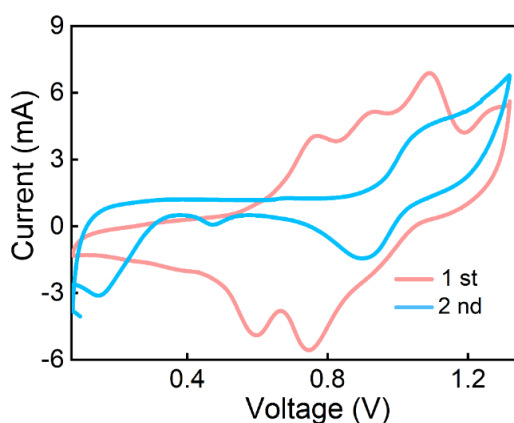


Figure S17. CV curves of C_3H_9IS/AC electrode.

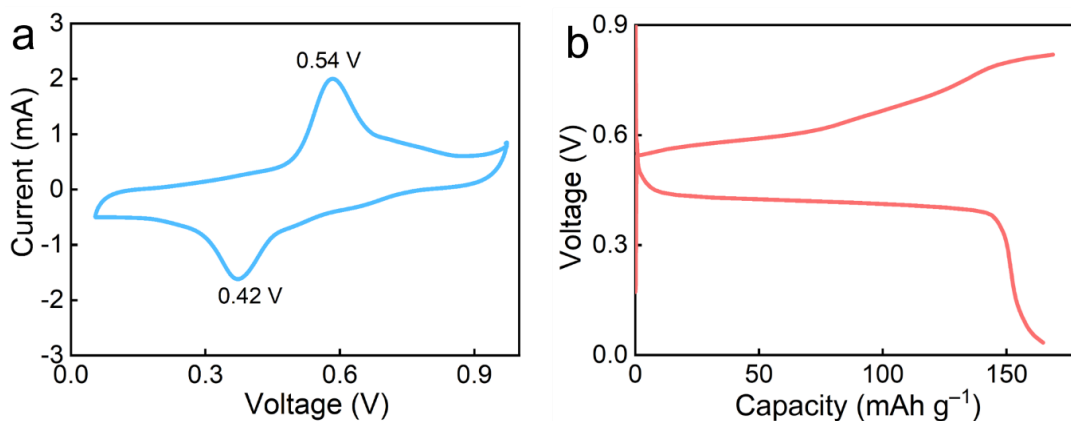


Figure S18. (a) CV and (b) GCD curve of $I_2/TZ-COFs$ electrode in aqueous $Zn(OTF)_2$ electrolyte.

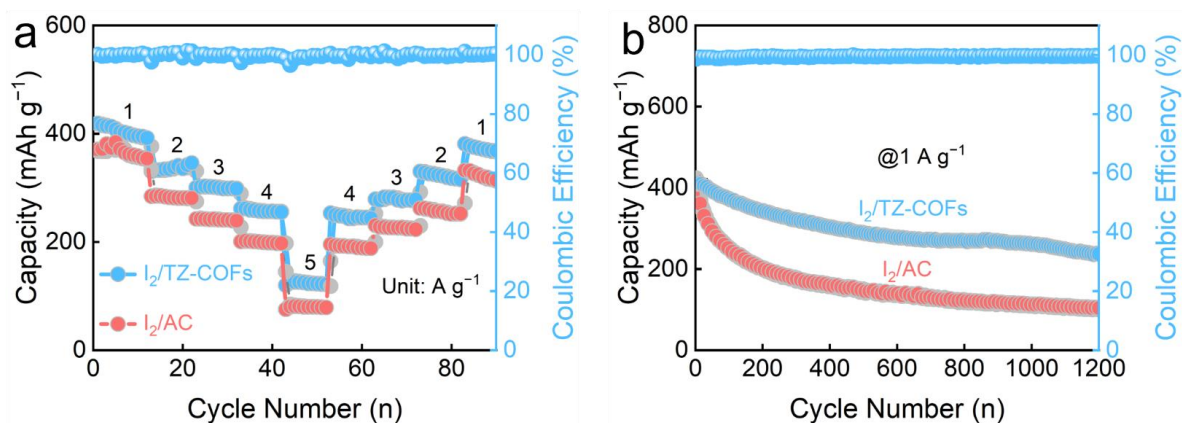


Figure S19. (a) Rate capacities and (b) cycling stability of I_2/AC and $I_2/TZ-COFs$ electrodes in $Zn(OTF)_2-MPIBr$ electrolyte.

Notes to Figure S19: $I_2/TZ-COFs$ electrode in $Zn(OTF)_2-MPIBr$ electrolyte delivers higher reversible rate capacities and cycling stability than that of I_2/AC electrode (Figure S19). This is because thiazole units of TZ-COFs enable strong chemical adsorption with IO_3^- species to improve redox stability with high reversibility due to reduced energy barriers (-5.1 vs. -3.5 eV in AC host, Figure 4f) and upgraded conversion kinetics (activation energy: 0.21 vs. 0.38 eV in AC, Figure 4g).

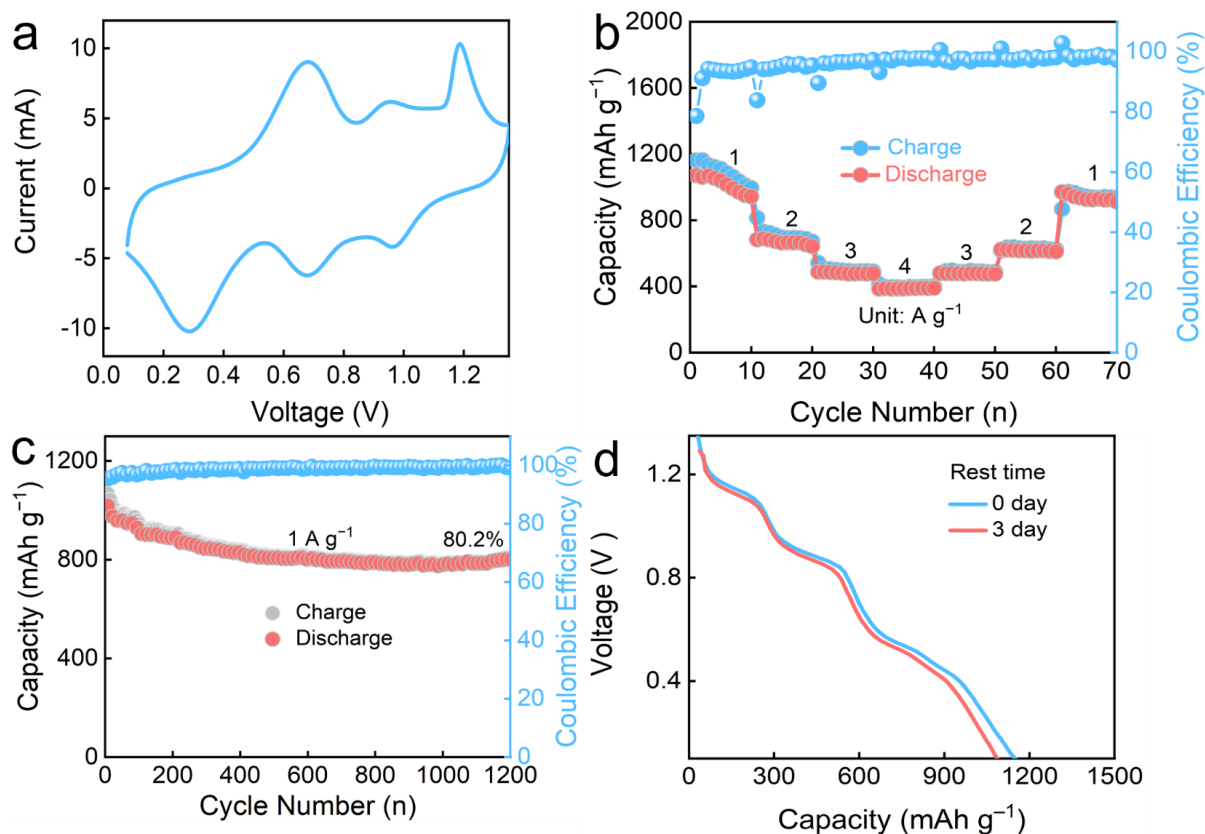


Figure S20. Electrochemical properties of $C_3H_9IS/TZ-COFs$ electrode in aqueous 3 M $ZnSO_4-MPIBr$ electrolyte. (a) CV curve, (b) rate capacities, (c) cycling stability and (d) self-discharge behavior.

Notes to Figure S20: For a comparison, the electrochemical properties of $C_3H_9IS/TZ-COFs$ electrode were tested in aqueous 3 M $ZnSO_4-MPIBr$ electrolyte (Figure S20). CV curve of $C_3H_9IS/TZ-COFs$ electrode in $ZnSO_4-MPIBr$ electrolyte exhibits three pairs of redox peaks at 0.54/0.42, 0.93/0.80, and 1.20/1.03 V, which is consistent with CV curve in $Zn(OTF)_2-MPIBr$ electrolyte, indicating the occurrence of I^- to IO_3^- conversion reactions. $C_3H_9IS/TZ-COFs$ electrode achieves a highly reversible capacity of 1156 mAh g^{-1} at 1 A g^{-1} and an energy density of 1387 Wh kg^{-1} (Figure S20b), as well as superior cycling stability (1000 cycles with 80.2% capacity retention, Figure S20c). The self-discharge behavior of Zn- I_2 battery is studied at the fully charged condition of 1.3 V, which shows a high-capacity retention of 92% after a rest step of 3 days.

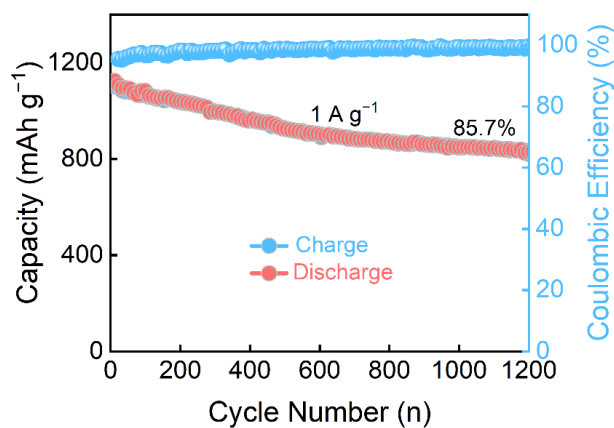


Figure S21. The capacity, Coulombic efficiency and cycling stability of Zn||C₃H₉IS/TZ-COFs battery.

Notes to Figure S21: The Zn||C₃H₉IS/TZ-COFs battery displays a high capacity, high Coulombic efficiency, as well as superior cycling stability.

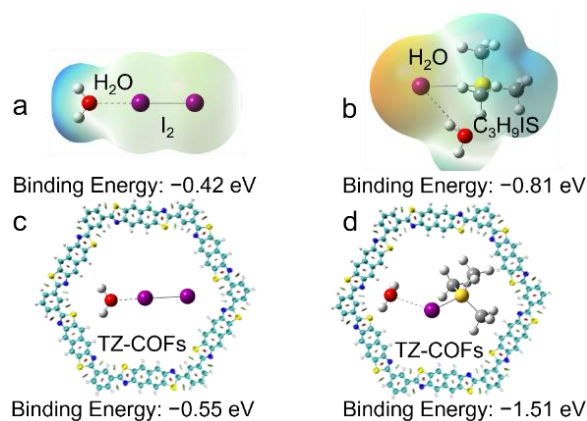


Figure S22. The binding energies of I₂ and C₃H₉IS with H₂O without (a, b) and with (c, d) TZ-COFs.

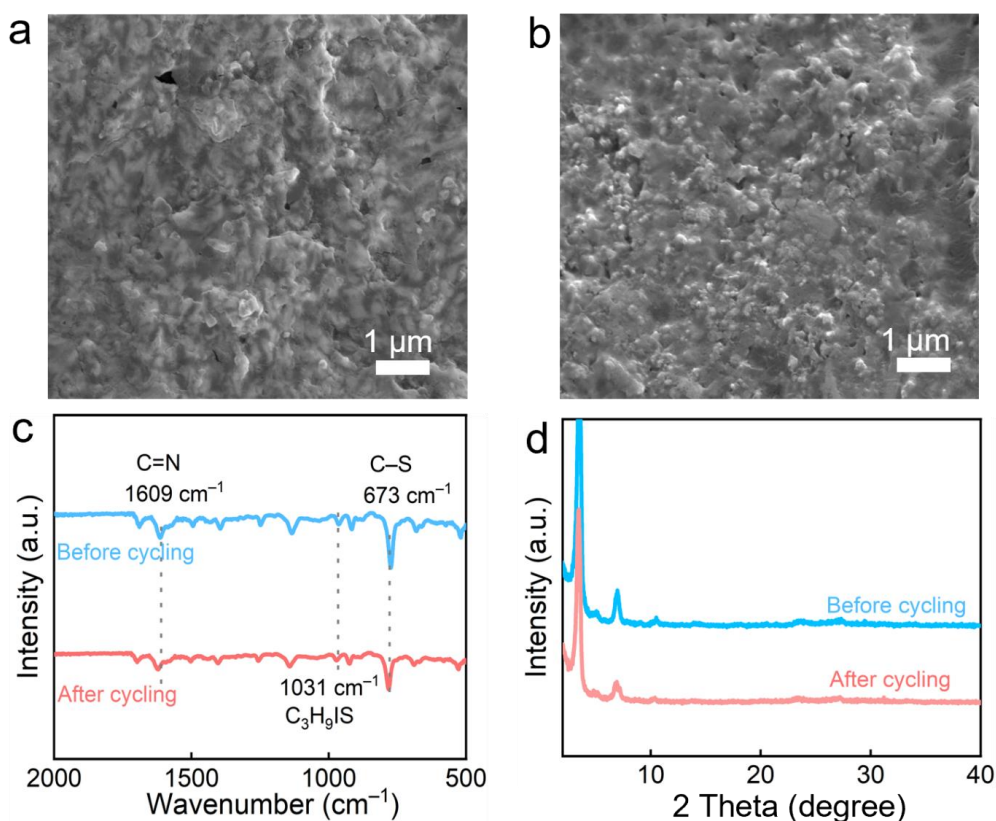


Figure S23. (a, b) SEM images, (c) FI-IR spectra and (d) XRD patterns of $C_3H_9IS/TZ-COFs$ electrode before and after cycling.

Notes to Figure S23: SEM images of cycled $C_3H_9IS/TZ-COFs$ electrode exhibit unchanged surface morphologies (Figure S23a and b), revealing its structural integrity during long-term (dis)charging cycles. Furthermore, FI-IR spectra of $C_3H_9IS/TZ-COFs$ electrode after cycling still exhibits strong electroactive signals of $C_3H_9S^+$ species in C_3H_9IS molecule at 1031 cm^{-1} and $C=N/C-S$ groups in $TZ-COFs$ at $1609/673\text{ cm}^{-1}$ (Figure S23c), confirming its functional robustness. Besides, $C_3H_9IS/TZ-COFs$ electrode shows identical XRD patterns before and after cycling (Figure S23d), suggesting its high structure regularity during the iodine conversion process. All these results support the stability of $C_3H_9IS/TZ-COFs$ electrode.

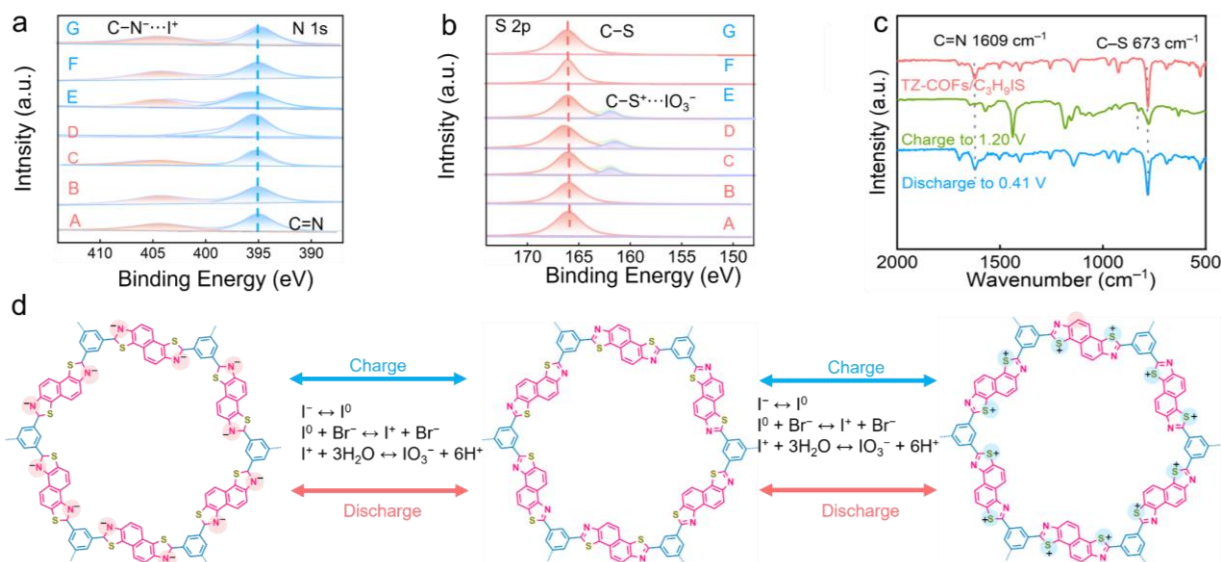


Figure S24. XPS spectra of (a) N 1s and (b) S 2p, (c) *ex-situ* FT-IR spectra of C₃H₉IS/TZ-COFs electrode at different (dis)charging states, (d) Absorption/desorption mechanism of different iodine species at C=N/C-S sites.

Notes to Figure S24: In N 1s XPS spectra (Figure S24a), a deconvoluted peak at 401.8 eV can be attributed to C=N groups of C₃H₉IS/TZ-COFs electrode at the initial state A. Upon charging (state B→D), the intensity of C=N moieties gradually decreased, accompanied by the appearance of electronegative C-N⁻ species due to the adsorption of I⁺ species, proving the chemical binding between C=N and I⁺ (C-N⁻...I⁺). In addition, a curve-fitted peak of C-S moieties at 168.2 eV can be observed at state A and B (Figure S24b), which undergoes a gradual decline during further charging (state C→D). Of note, a new peak of electropositive C-S⁺ species at 163.9 eV emerges, which derives from the adsorption of IO₃⁻ species (C-S⁺...IO₃⁻). During the discharge process (state D→G), all signals return to their initial states owing to removal of different iodine species from C=N/C-S sites in C₃H₉IS/TZ-COFs electrode. Besides, C=N/C-S groups of C₃H₉IS/TZ-COFs electrode in FT-IR spectra shows reversible attenuation/enhancement during (dis)charging due to the adoption/desorption of iodine species (Figure S24c). Overall, different iodine species get adsorbed into C₃H₉IS/TZ-COFs electrode via strong chemical binding (C=N/C-S...I) to trigger multielectron I⁻/I⁰/I⁺/I⁵⁺ redox reactions (Figure S24d).

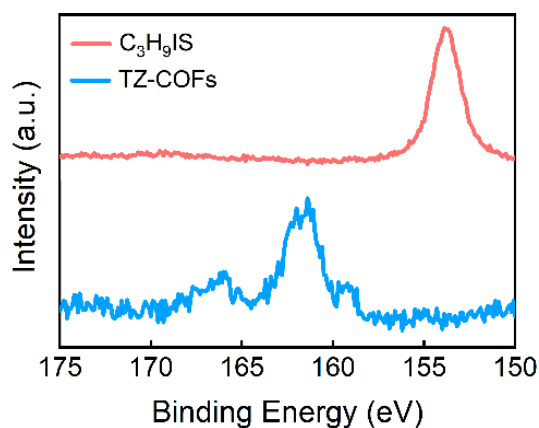


Figure S25. S 2p XPS spectra of C₃H₉IS and TZ-COFs.

Notes to Figure S25: The C–S bonds in C₃H₉S⁺ and TZ-COFs are located at 155 eV and 165 eV, respectively. The characteristic peak of C–S group in TZ-COFs at 165 eV shifts to higher binding energy during charging (Figure S24b), demonstrating their redox activity with iodine species.

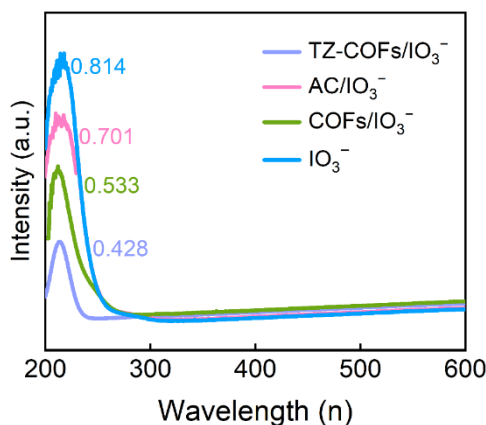


Figure S26. UV-vis absorbance spectra of TZ-COFs, COFs and AC to IO₃⁻.

Notes to Figure S26: HIO₃ as a presentative source of IO₃⁻ was added in Zn(OTF)₂ electrolyte, which was then separately immersed with TZ-COFs, COFs and AC for 7 days for UV-vis spectra test. TZ-COFs shows an adsorption concentration of $3.68 \times 10^{-5} \text{ mol L}^{-1}$, which is higher than those of COFs ($3.45 \times 10^{-5} \text{ mol L}^{-1}$) and AC ($1.59 \times 10^{-6} \text{ mol L}^{-1}$), indicating its strong adsorption ability for IO₃⁻.

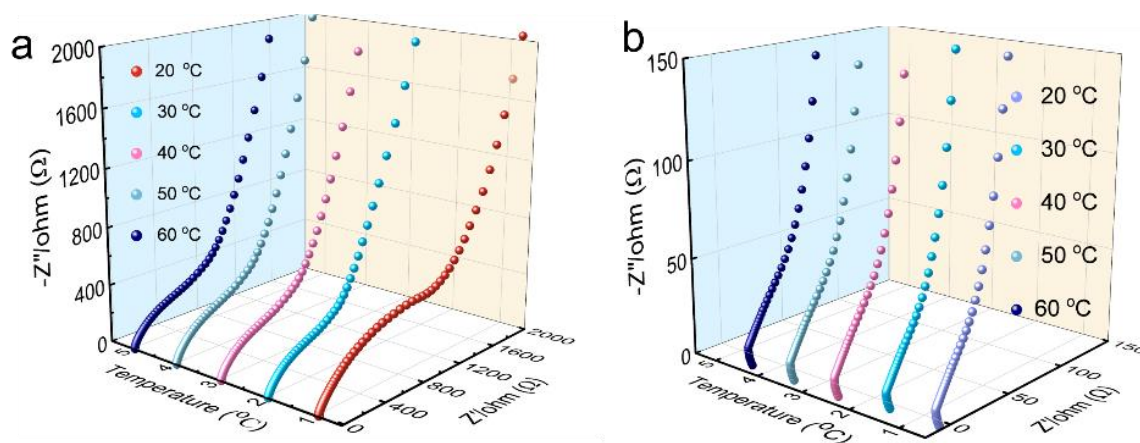


Figure S27. EIS spectra of (a) C₃H₉IS/AC and (b) C₃H₉IS/TZ-COFs electrodes.

Table S1. Performance comparison of Zn-I₂ batteries.

Strategy	Electrode	Electrolyte	C _m (mAh g ⁻¹)	Cycle (n)	V (V)	E (Wh kg ⁻¹)	Refs.
I ⁻ /IO ₃ ⁻	C ₃ H ₉ IS/TZ-COFs	Zn(OTF) ₂ -MPIBr	1296	1200	1.1 3	1464	This work
I ⁻ /IO ₃ ⁻	HAC/I ₂	H ₂ SO ₄ +KBr	1200	70	1.1 3	1357	[S10]
I ⁻ /IO ₃ ⁻	Carbon felt	HI+KBr+H ₂ SO ₄	945	1000	1.4 3	1350	[S11]
I ⁰ /I ⁺	HAC/I ₂	ZnSO ₄ +ZnCl ₂	594	6000	1.2	750	[S12]
I ⁰ /I ⁺	Co ₉ S ₈ @NC	ZnCl ₂	458	5000	1.2	554	[S13]
I ⁰ /I ⁺	Ni-Fe-I LDH	ZnSO ₄ + ZnBr ₂	350	10000	1.2	N/A	[S14]
I ⁰ /I ⁺	I ₂	CuSO ₄ + CuCl ₂	560.4	500	1.2	N/A	[S15]
I ⁰ /I ⁺	ODASnI ₄	ZnSO ₄ +LiCl	246	2000	1.2	N/A	[S16]
I ⁰ /I ⁺	TmdpPb ₂ [IBr] ₆	ZnSO ₄	336	4000	1.2	441	[S17]
I ₃ ⁻	PIL	ZnCl ₂	5.04	200	1.1	N/A	[S18]

mAh cm ⁻²							
I ₃ ⁻	LA ₁₃₃ /I ₂	ZnSO ₄ + Li ₂ SO ₄	202.8	1000	1.1	N/A	[S19]
I ⁰ /I ⁺	NA	Zn(ClO ₄) ₂ +NA+ DMS	412	2000	1.0	404	[S20]
I ⁰ /I ⁺	CC-I ₂	ZnSO ₄ + LiBr+LiNO ₃	608	500	1.2	3.11mWh cm ⁻²	[S21]
I ⁰ /I ⁺	PTCDI	KCl+ZnCl ₂	900	90000	1.2	434	[S22]
I ₃ ⁻	HCNT-O	CPAM-Zn-I-0.5	193.3 μAh cm ⁻²	2600	1.1	1647.3 mWh cm ⁻³	[S23]
I ₃ ⁻	Zn-PCA	ZnSO ₄	211	30000	1.1	N/A	[S24]
I ₂ /I ⁻	Nb ₂ CTX	ZnSO ₄	143	25000	1.1	259.3	[S25]
I ₃ ⁻	CNF	ZnSO ₄	182.7	3000	1.1	521.2	[S26]
I ₃ ⁻	IL-ZIF-90)	ZnSO ₄	120.3	65000	1.1	N/A	[S27]
I ₃ ⁻	mPD@rGO	Zn(CF ₃ SO ₃) ₂	271.4	35000	1.1	N/A	[S28]

Section S4. References

- [S1] K. Wang, Z. Jia, Y. Bai, X. Wang, S. E. Hodgkiss, L. Chen, S. Y. Chong, X. Wang, H. Yang, Y. Xu, F. Feng, J. W. Ward, A. I. Cooper, *J. Am. Chem. Soc.* **2020**, *142*, 11131.
- [S2] P. E. Blöchl, O. Jepsen, O. K. Andersen, *Phys. Rev. B* **1994**, *49*, 16223.
- [S3] P. Giannozzi, O. Andreussi, T. Brumme, O. Bunau, M. Buongiorno Nardelli, M. Calandra, R. Car, C. Cavazzoni, D. Ceresoli, M. Cococcioni, N. Colonna, I. Carnimeo, A. Dal Corso, S. de Gironcoli, P. Delugas, R. A. DiStasio, A. Ferretti, A. Floris, G. Fratesi, G. Fugallo, R. Gebauer, U. Gerstmann, F. Giustino, T. Gorni, J. Jia, M. Kawamura, H. Y. Ko, A. Kokalj, E. Küçükbenli, M. Lazzeri, M. Marsili, N. Marzari, F. Mauri, N. L. Nguyen, H. V. Nguyen, A. Otero-de-la-Roza, L. Paulatto, S. Poncé, D. Rocca, R. Sabatini, B. Santra, M. Schlipf, A. P. Seitsonen, A. Smogunov, I. Timrov, T. Thonhauser, P. Umari, N. Vast, X. Wu, S. Baroni, *J. Phys.: Condens. Matter* **2017**, *29*, 465901.
- [S4] P. Giannozzi, S. Baroni, N. Bonini, M. Calandra, R. Car, C. Cavazzoni, D. Ceresoli, G. L. Chiarotti, M. Cococcioni, I. Dabo, A. Dal Corso, S. de Gironcoli, S. Fabris, G. Fratesi, R. Gebauer, U. Gerstmann, C. Gougoussis, A. Kokalj, M. Lazzeri, L. Martin-Samos, N.

- Marzari, F. Mauri, R. Mazzarello, S. Paolini, A. Pasquarello, L. Paulatto, C. Sbraccia, S. Scandolo, G. Sclauzero, A. P. Seitsonen, A. Smogunov, P. Umari, R. M. Wentzcovitch, *J. Phys.: Condens. Matter* **2009**, *21*, 0953-8984.
- [S5] P. Hu, X. He, M. F. Ng, J. Ye, C. Zhao, S. Wang, K. Tan, A. Chaturvedi, H. Jiang, C. Kloc, W. Hu, Y. Long, *Angew. Chem. Int. Ed.* **2019**, *58*, 13513.
- [S6] E. Torres, T. P. Kaloni, *Comput. Mater. Sci.* **2020**, *171*, 109237.
- [S7] Z. Song, L. Miao, Y. Lv, L. Gan, M. Liu, *Angew. Chem. Int. Ed.* **2023**, *62*, e202309446.
- [S8] Z. Song, L. Miao, H. Duan, L. Ruhlmann, Y. Lv, D. Zhu, L. Li, L. Gan, M. Liu, *Angew. Chem. Int. Ed.* **2022**, *61*, e202208821.
- [S9] a) J. W. Ypenburg, E. van Der Leij-Van Wirdum, H. Gerding, *Recueil des Travaux Chimiques des Pays-Bas*. **1971**, *90*, 896-900; b) J. A. Creighton, J. H. S. Green, D. J. Harrisson, S. M. Waller, *Spectrochimica Acta Part A: Molecular Spectroscopy*. **1967**, *23*, 2973-2979.
- [S10] W. Ma, T. Liu, C. Xu, C. Lei, P. Jiang, X. He, X. Liang, *Nat. Commun.* **2023**, *14*, 5508.
- [S11] C. Xie, C. Wang, Y. Xu, T. Li, Q. Fu and X. Li, *Nature Energy*, 2024, **9**, 714–724.
- [S12] Y. Zou, T. Liu, Q. Du, Y. Li, H. Yi, X. Zhou, Z. Li, L. Gao, L. Zhang, X. Liang, *Nat. Commun.* **2021**, *12*, 170.
- [S13] T. Hu, Y. Zhao, Y. Yang, H. Lv, R. Zhong, F. Ding, F. Mo, H. Hu, C. Zhi, G. Liang, *Adv. Mater.* **2024**, *36*, 2312246.
- [S14] C. Wang, X. Ji, J. Liang, S. Zhao, X. Zhang, G. Qu, W. Shao, C. Li, G. Zhao, X. Xu, H. Li, *Angew. Chem. Int. Ed.* **2024**, *63*, e202403187.
- [S15] S. Bi, H. Wang, Y. Zhang, M. Yang, Q. Li, J. Tian, Z. Niu, *Angew. Chem. Int. Ed.* **2023**, *62*, e202312982.
- [S16] X. Li, S. Wang, D. Zhang, P. Li, Z. Chen, A. Chen, Z. Huang, G. Liang, A. L. Rogach, C. Zhi, *Adv. Mater.* **2024**, *36*, 2304557.
- [S17] S. Wang, Y. Wang, Z. Wei, J. Zhu, Z. Chen, H. Hong, Q. Xiong, D. Zhang, S. Li, S. Wang, Y. Huang, C. Zhi, *Adv. Mater.* **2024**, *36*, 2401924.
- [S18] H. Zhao, D. Yin, Y. Qin, X. Cui, J. Feng, Y. Zhang, L. Zhao, N. Gao, M. Cui, C. Xiao, G. Feng, Y. Su, K. Xi, S. Ding, *J. Am. Chem. Soc.* **2024**, *146*, 6744.
- [S19] K. Wang, H. Li, Z. Xu, Y. Liu, M. Ge, H. Wang, H. Zhang, Y. Lu, J. Liu, Y. Zhang, Y. Tang, S. Chen, *Adv. Energy Mater.* **2024**, *14*, 2304110.
- [S20] W. Li, H. Xu, H. Zhang, F. Wei, T. Zhang, Y. Wu, L. Huang, J. Fu, C. Jing, J. Cheng, S. Liu, *Energy Environ. Sci.* **2023**, *16*, 4502.
- [S21] S. Lv, T. Fang, Z. Ding, Y. Wang, H. Jiang, C. Wei, D. Zhou, X. Tang, X. Liu, *ACS Nano* **2022**, *16*, 20389.
- [S22] Z. Zhang, Y. Zhu, M. Yu, Y. Jiao, Y. Huang, *Nat. Commun.* **2022**, *13*, 6489.
- [S23] X. Jin, L. Song, C. Dai, Y. Xiao, Y. Han, X. Li, Y. Wang, J. Zhang, Y. Zhao, Z. Zhang, N.

- Chen, L. Jiang, L. Qu, *Adv. Mater.* **2022**, *34*, 2109450.
- [S24] F. Wang, W. Liang, X. Liu, T. Yin, Z. Chen, Z. Yan, F. Li, W. Liu, J. Lu, C. Yang, Q.-H. Yang, *Adv. Energy Mater* **2024**, *14*, 2400110.
- [S25] X. Li, N. Li, Z. Huang, Z. Chen, G. Liang, Q. Yang, M. Li, Y. Zhao, L. Ma, B. Dong, Q. Huang, J. Fan, C. Zhi, *Adv. Mater.* **2021**, *33*, e2006897.
- [S26] Z. Li, W. Cao, T. Hu, Y. Hu, R. Zhang, H. Cui, F. Mo, C. Liu, C. Zhi, G. Liang, *Angew. Chem. Int. Ed.* **2024**, *63*, e202317652.
- [S27] J. He, Y. Mu, B. Wu, F. Wu, R. Liao, H. Li, T. Zhao, L. Zeng, *Energy Environ. Sci.* **2024**, *17*, 323.
- [S28] F. Wei, T. Zhang, H. Xu, Y. Peng, H. Guo, Y. Wang, S. Guan, J. Fu, C. Jing, J. Cheng, S. Liu, *Adv. Funct. Mater.* **2024**, *34*, 2310693.